Materials Science & Engineering A 807 (2021) 140862

Contents lists available at ScienceDirect

Materials Science & Engineering A

journal homepage: http://www.elsevier.com/locate/msea

Linking mechanical properties to precipitate microstructure in three Al-Mg-Si(-Cu) alloys

Jonas K. Sunde [a], Feng Lu [b], Calin D. Marioara [c], Bjørn Holmedal [b], Randi Holmestad [a,*]

[a] Department of Physics, Norwegian University of Science and Technology (NTNU), N-7491, Trondheim, Norway
[b] Department of Materials Science and Engineering, NTNU, N-7491, Trondheim, Norway
[c] Materials and Nanotechnology, SINTEF Industry, N-7465, Trondheim, Norway

ARTICLE INFO

Keywords:
6xxx Al alloys
Precipitation
Yield strength
Transmission electron microscopy
Strengthening models
Microstructure-property relationships

ABSTRACT

The mechanical properties of age hardenable Al alloys depend strongly on the precipitate microstructure. This work has investigated the relationship between properties such as strength and ductility and the distribution of precipitates, using three Al-Mg-Si(-Cu) alloys (Cu≲0.1 at.%). A range of ageing conditions was examined in order to understand the effect of an evolving precipitate microstructure, and the results were used as input for strengthening models. The mechanical properties were obtained by tensile tests and microstructure characterisation was attained by transmission electron microscopy. The results showed that minor changes to the Si, Mg, and Cu additions – the total addition (at.%) kept approximately equal – had a significant impact on material properties, with corresponding changes in the precipitate microstructure. On the peak strength plateaus differences as large as 35 MPa in yield strength were measured between the strongest and the weakest alloy, obtained as 410 MPa and 375 MPa, respectively. Higher material yield strength correlated well with a refined precipitate microstructure comprising higher number densities of smaller precipitates. Differences with respect to material ductility first appeared after moderate overageing of the alloys, showing negative correlation with material strength. At significantly overaged conditions the differences in strength exceeded 100 MPa, demonstrating large differences with respect to the thermal stability of these materials, which has important consequences for alloys exposed to elevated temperatures under in-service conditions. The highly comprehensive body of data presented here should serve as a valuable reference in the development of precipitation and strengthening models for the Al-Mg-Si-Cu system and will hopefully incite further investigations on the topics covered.

1. Introduction

The AA6xxx series Al-Mg-Si(-Cu) alloys contain important age hardenable alloys for extruded products in automotive, marine, and building construction applications. They are widely used due to their low cost, high machinability, and to a combination of attractive material properties, including high strength, low weight, nice surface finish, and good corrosion resistance. The strongest AA6xxx series Al alloys, e.g. 6082, are becoming increasingly utilised in the crash-system and the steering components of automotive vehicles [1]. It is here important to optimise the collision properties of these materials. A high yield strength, σ_y, is crucial in order to resist deformation. The ability to work harden and the fracture strain, ε_f, affect the energy absorption capacity. For automotive components that will be exposed to elevated temperatures under in-service conditions the thermal stability is important, and the change of σ_y with prolonged ageing is highly relevant in this regard.

The strength of these alloys is caused by the formation and growth of a high density of nanosized rod- and/or lath-shaped precipitate phases with long axes parallel to $\langle 100 \rangle_{Al}$, acting as obstacles to dislocation motion. Depending on alloy composition and thermomechanical processing (TMP) various precipitate phases may form. The phases of the Al-Mg-Si- and the Cu-added system have been thoroughly characterised [2–5]. Changes in composition and TMP will also affect the distribution and size of precipitates, which will have a direct influence on material properties.

Considerable research efforts in the past have been made to understand the connection between the precipitate microstructure and the mechanical properties of Al-Mg-Si-Cu alloys [6–16]. One of the fundamental interactions that determine the mechanical properties of age hardenable Al alloys is that occurring between precipitates and moving

* Corresponding author.
E-mail address: randi.holmestad@ntnu.no (R. Holmestad).

https://doi.org/10.1016/j.msea.2021.140862
Received 13 October 2020; Received in revised form 19 January 2021; Accepted 25 January 2021
Available online 3 February 2021
0921-5093/© 2021 The Authors. Published by Elsevier B.V. This is an open access article under the CC BY license (http://creativecommons.org/licenses/by/4.0/).

Table 1
Compositions of the Al-Mg-Si(-Cu) alloys studied. The last column shows the estimated total concentrations of precipitate forming elements left in solid solution immediately after quenching.

Alloy	Al	Si	Mg	Cu	Fe	Mn	Cr	Si[a] + Mg + Cu
S at./wt. %	bal.	0.85/0.88	0.80/0.72	0.01/0.03	0.12/0.24	0.25/0.51	0.08/0.16	1.52/1.44
C at./wt. %	bal.	0.85/0.88	0.71/0.64	0.04/0.09	0.10/0.20	0.22/0.45	0.07/0.14	1.46/1.42
M at./wt. %	bal.	0.62/0.64	0.86/0.77	0.10/0.23	0.13/0.23	0.13/0.26	0.01/0.02	1.46/1.48

[a] The incorporation of Si into dispersoids was taken into account using an estimate based on the thermal history of the material and the Alstruc microstructure solidification model [26].

dislocations. Al has a fcc crystal lattice, causing dislocations with Burgers vector in close packed $\langle 110 \rangle_{Al}$ directions to glide on $\{111\}_{Al}$ planes. There are two main types of precipitate-dislocation interactions. Either mobile dislocations pass through the precipitate (shearable), or they bypass the precipitate, e.g. via Orowan looping (non-shearable) [6–8]. Whether a particular precipitate is sheared or bypassed depends on several factors, where interface coherence and cross-section area on the $\{111\}_{Al}$ slip planes are the most important.

Up to the peak hardened state the most common precipitate phase existing in the microstructure of Al-Mg-Si alloys is the needle-shaped β'' phase [17]. In alloys that are Mg-rich (Mg/Si (at.%) > 1) and that contain a low addition of Cu (0.05–0.3 Cu at.%), β'' may coexist with the lath-shaped L phase [1,5,18]. *In situ* investigations performed on an Al-Mg-Si-Cu alloy containing both β'' and L phases suggest that both shearing and bypassing of precipitates occur at room temperature, and that increasing temperature facilitates bypassing by cross-slip [19,20]. Which of the β'' or L phase precipitates are sheared/bypassed was not determined, but there exists strong evidence that β'' is shearable [21–24]. In overaged conditions the precipitates are to a larger extent non-shearable [25], i.e. they remain undeformed while the matrix around them is deformed. Typical phases existing in overaged, low Cu containing Al-Mg-Si alloys are β', Q′ and L phase [5]. Several studies have made attempts to estimate the value of the critical dimension that determines the transition point between shearable and non-shearable precipitates for the various precipitate phases existing in this alloy system, e.g. Refs. [23,25]. The critical dimension, r_c, where this transition occurs is important in order to model the strength in these alloys, as the obstacle strength, $F(r)$, is usually separated into a weak ($r \leq r_c$) and strong ($r > r_c$) regime.

Despite the complexity of the underlying strengthening mechanisms, many yield strength models developed for Al-Mg-Si-Cu alloys capture the general evolution of material strength with ageing to a reasonable extent. The crudest models assume a single precipitate type approximated as equivalent spherical volumes, whereas more advanced models also take into account the $\langle 100 \rangle_{Al}$ oriented, rod-/lath-shaped nature of the precipitates and their size distribution.

This work studies three Al-Mg-Si(-Cu) alloys with nearly equal total alloying additions (at.%). Mechanical properties were inferred from tensile tests and precipitate statistics were calculated from transmission electron microscopy (TEM) results. Given numerous previous developments in the modelling of material strength for Al-Mg-Si-Cu alloys, we saw the need for making a comparison between important models developed within the field. To this point, we chose here to compare experimental findings with the models developed by O. R. Myhr et al. [11], S. Esmaeili et al. [13] and B. Holmedal [15]. The combination of extensive materials testing, characterisation, and modelling work provided a comprehensive evaluation of microstructure-property relationships existing in these alloys.

2. Experimental details

2.1. Materials and heat treatments

Three Al-Mg-Si(-Cu) alloys labelled S, C, and M were designed with similar total alloying additions (at.%) and minor differences in the Si:Mg ratios and Cu content, see Table 1, [26]. The alloys were provided by Neuman Aluminium Raufoss as extruded rods (Ø30 mm). 10 mm height cylinder specimens, cut perpendicular to the extrusion direction, were given a solution heat treatment (SHT) at 540 °*C* for 12 min in a salt bath, and then water-quenched to room temperature. The specimens were kept at room temperature for 10 min before artificial ageing (AA) at 180 °*C* in an oil bath. AA was conducted for a series of holding times from 20 min to 1 month total ageing, which spanned underaged (UA) – through peak aged – to significantly overaged (OA) material conditions. A schematic of the heat treatment procedure is shown in Fig. 1.

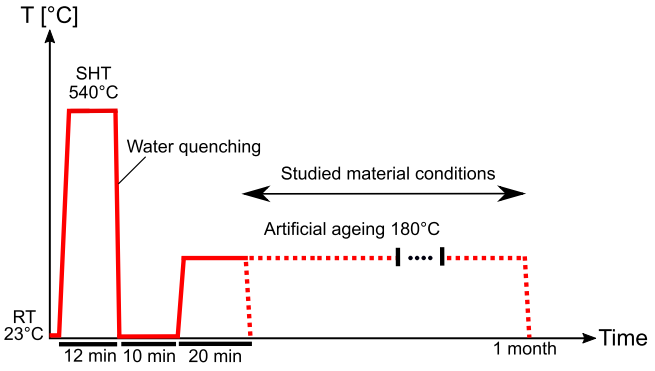

Fig. 1. Heat treatment procedure applied for the studied Al-Mg-Si(-Cu) alloys.

2.2. Mechanical testing and electrical conductivity

The cylinder specimens were used for serial hardness and electrical conductivity measurements after different ageing times. Vickers hardness tests were carried out on a Leica VMHT MOT hardness tester using an applied load of 1 kg. 10 indentation marks were inserted concentrically on the top face of the cylinder, a few mm from outer edge and centre, and formed the basis for calculating the average value for each ageing condition. Electrical conductivity was measured using a Foerster Sigmatester 2.069. Each value was determined as the average of 5 measurements on the specimen surface.

Tensile tests were conducted on cylindrical specimens with 18 mm gauge length and Ø6 mm diameter pulled parallel to the extrusion direction. The specimens were machined from the centre part of the extruded rods and the dimensions are shown in Fig. 2. A universal tensile test machine and an optical measurement technique [27] were employed for the tensile testing. The tests were conducted at room temperature using a load speed of 0.54 mm/min, and 3 parallel

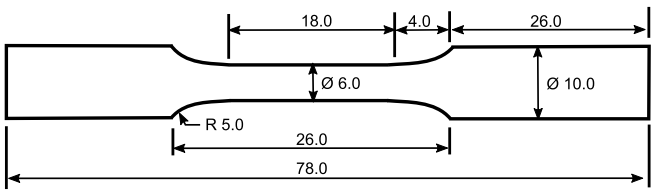

Fig. 2. Dimensions in mm for tensile test specimens.

specimens were tested in order to get the average value of the tensile properties. The radius of the minimal cross-section area, a, the curvature radius of the necking region, R, and the corresponding load were measured using the optical measurement technique during experiments. These parameters were used as inputs for the Gromada necking correction approach [28] and the corrected stress-strain curve until fracture was then calculated for each condition. Material yield strength, σ_y, was obtained from the curves using the 0.2% offset method. True strain, ε, was estimated from the measurements of radius, a, by assuming volume consistency. The fracture strain was obtained at the occurrence of fracture for each condition, $\varepsilon_f = \ln(A_0/A_f) = 2\ln(a_0/a_f)$, where A denotes the cross-section area in the necking region (subscript 0 = initial, f = at fracture).

2.3. Electron microscopy

Thin foils for TEM experiments were prepared by further cutting and grinding the cylinder specimens used for hardness/conductivity measurements, down to disks with thicknesses of about 100 μm, and then punching them into several smaller Ø3 mm disks. Twin-jet polishing in a Struers Tenupol-5 was used to further thin the disks to electron transparency. The electrolytic solution comprised a 2:1 mixture of methanol: nitric acid maintained at roughly −25 °C.

Precipitate statistics were obtained using a JEOL 2100 microscope operated at 200 kV and equipped with a Gatan Imaging Filter. The specimen thickness was measured by electron energy loss spectroscopy (EELS) using the t/λ (log-ratio) methodology with an electron mean free path $\lambda \approx 130$ nm for 200 keV electrons in the $\langle 100 \rangle_{Al}$ zone axis of fcc Al. Existing methodologies in microstructure quantification of Al alloys by TEM give precipitate dimensions and distributions [29], including precipitate number density, N, length, l, cross-section area, a, and volume fraction, V_f. The width of precipitate free zones (PFZs) perpendicular to grain boundaries (GBs) were determined from annular dark-field scanning TEM (ADF-STEM) images obtained on a JEOL 2100F microscope (200 kV).

3. Results

3.1. Hardness and electrical conductivity

The hardness and the electrical conductivity of the alloys at different ageing times are shown in Fig. 3. It is seen that alloys C and M both started out higher in hardness than alloy S, and after 10 min ageing these were at roughly 80 compared to 65 HV, respectively. Subsequently, all alloys showed a similar rate of hardness increase, all reaching close to peak hardness after roughly 2 h ageing, with values ranging from 122 HV for alloy S to 128 HV for alloy M. The hardness then remained nearly constant, and all alloys exhibited a similar duration in the peak hardness plateau, from approximately 2 h–12 h ageing. At 12 h ageing, alloys S and C exhibited comparable hardness values, 122 HV, and the rate of hardness decrease with following overageing was similar in the two alloys. After 4 days of ageing there had again developed a significant hardness difference between alloys S and C, and beyond this point alloy C stayed roughly 8 HV higher than for alloy S.

With overageing alloy M differed strikingly from alloys S and C. At 12 h ageing alloy M measured 126 HV, and with further ageing it maintained a substantially higher hardness than alloys S and C for all subsequent conditions, indicating a considerably improved thermal stability. After roughly 5 days ageing the hardness difference relative to alloys S and C was at a maximum, and it stayed nearly unchanged with further ageing. At 5 days ageing and onwards, the hardness difference was near 19 HV relative to alloy C, and about 23 HV to alloy S. After 1 month accumulated ageing, the hardness of alloys S and C measured 70 and 75 HV, respectively, which was within 5 HV of their corresponding 10 min ageing measurements. Alloy M measured 94 HV at 1 month ageing, which was still significantly higher than the 10 min value at ≈ 80 HV.

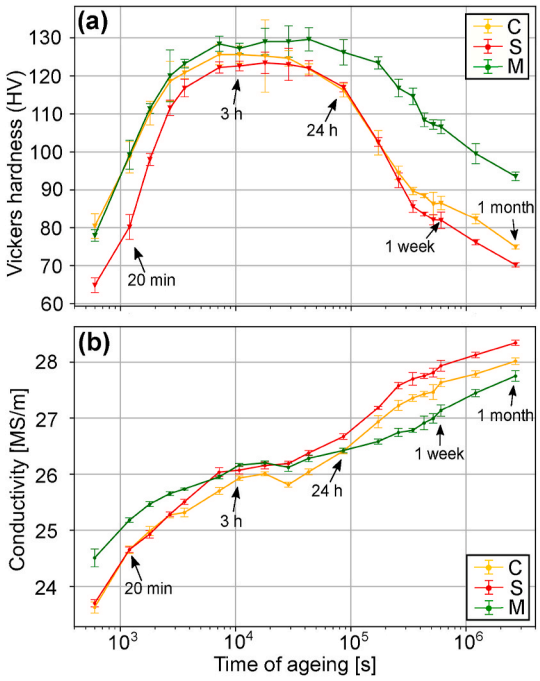

Fig. 3. (a) Vickers hardness (HV) and (b) electrical conductivity after different ageing times at 180 °C.

The electrical conductivity of alloy M started out at 24.4 MS/m after 10 min ageing, higher than both alloys S and C at ≈23.5 MS/m. Further, the conductivity of alloys S and C increased at a higher rate than for alloy M. Near peak hardness (≈ 3h) all alloys exhibited similar conductivity values, measuring roughly 26 MS/m. Beyond moderate overageing (> 24h) the ordering high-to-low was reversed relative to the hardness at corresponding ageing times. The ordering high-to-low in terms of conductivity was here: alloy S, alloy C, and alloy M. Final values reached after 1 month ageing were 28.3, 28.0, and 27.7 MS/m for alloys S, C, and M, respectively.

The material conditions selected for TEM experiments were chosen based of the plots in Fig. 3, and are shown in Table 2. With the aim to understand the influence of an evolving microstructure on the overall strength and ductility of the material, a range of conditions was selected, encompassing UA, peak hardened, and significantly OA material conditions.

3.2. Tensile properties

Tensile tests were performed on several material conditions, including all conditions selected for TEM studies. The true stress-strain curves for all ageing conditions in each alloy are shown in the Supplementary Information (SI) in section SI 1 (Fig. SI 1, Fig. SI 2, and Fig. SI 3), with following tables (Table SI 1, Table SI 2, and Table SI 3) showing the parameters of the fitted 4-term Voce equation for each curve. The main results obtained from the true stress-strain curves are presented in Fig. 4, showing the material yield strength, σ_y, and the true fracture strain, ε_f.

The main trends of the σ_y-plot in Fig. 4a show good agreement with

Table 2
Ageing conditions selected for TEM experiments.

Alloy	Time of ageing at 180 °C
S	20 min, 3 h, 12 h, 24 h, 1 week, 2 weeks, 1 month
C	20 min, 3 h, 12 h, 24 h, 3 days, 1 week
M	20 min, 3 h, 24 h, 1 month

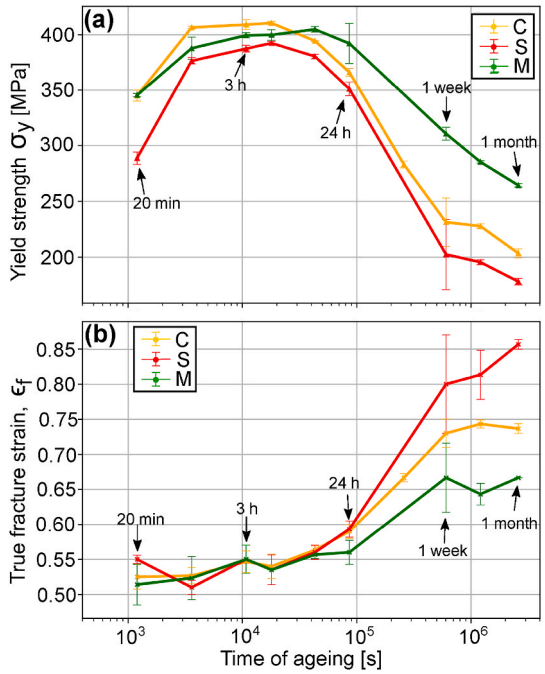

Fig. 4. Material tensile properties obtained from true stress-strain curves, showing (a) yield strength and (b) true fracture strain after different ageing times at 180 °C.

the Vickers hardness plot in Fig. 3a. One exception is due to alloy C, which in the σ_y-plot is no longer sandwiched in-between alloys S and M in value. At UA and peak aged conditions alloy C obtained highest σ_y-values, with a peak value of 410 MPa at 5 h ageing, compared to 392 MPa (5 h) and 406 MPa (12 h) for alloys S and M, respectively. In agreement with measured hardness, alloy M reigned supreme at OA conditions (> 12 h). At significantly OA conditions (> 1 week), alloy M stayed roughly 60 and 100 MPa higher in σ_y as compared to alloys C and S, respectively. Alloy C stayed close to- but exhibited consistently higher σ_y than alloy S with overageing. σ_y at 20 min ageing was also notably higher than the value at significantly OA conditions (> 1 week ageing) for all alloys. In the case of hardness, these outer extremes of UA vs OA values were closer, with the exception of alloy M.

True fracture strain, ε_f, remained comparable for all alloys (51%–55%) up to the onset of overageing, at about 12 h. Beyond this point the differences became progressively larger, and the ordering high-to-low was alloy S, C, and M, respectively, reversed with respect to the σ_y-ordering at corresponding conditions. Final values reached after 1 month ageing were 86% for alloy S, 74% for alloy C, and 67% for alloy M.

3.3. Quantification of precipitate statistics by TEM

Bright-field TEM images of the precipitate microstructures in the three alloys after various ageing times are shown in Fig. 5. At 20 min ageing (Fig. 5a–c), a highly dense microstructure of atomic clusters/GP-zones and small precipitates existed, with main growth dimension rarely exceeding 9 nm in length for all alloys. Near the peak hardened state at 3 h ageing (Fig. 5d–f), the microstructures comprised high densities of short β'' phase precipitates with characteristic strain contrast (dark lines) running parallel to the main growth direction. In alloy M, longer and narrower lath-shaped L phase precipitates were also present (highlighted). After 1 week ageing, the precipitates in alloys S and C had grown very large as compared to the 3 h condition (Fig. 5g and h). In addition, the precipitate density had been reduced significantly as expected for OA conditions. The precipitates in alloy M demonstrated a high resistance towards coarsening, and at 1 month ageing (Fig. 5i) their average size was still smaller than the precipitates at the 1 week ageing condition in alloys S and C. The development in average precipitate cross-section areas and lengths are shown in Fig. 6. From the 3 h ageing condition and onwards, it was relatively straightforward to classify the cross-sections as either lath-type or rod-type. Narrow, lath-shaped cross-sections extended along $[010]_{Al}$ and $[100]_{Al}$ directions were visible in both alloy C and M (highlighted). It was clear that the lath-type precipitates were more frequent in alloy M. Lath-shaped precipitates are either L phase or C phase precipitates [30]. The rod-type precipitates present were mainly β'', β', and Q′ phase precipitates. It is important to note that a Q′ phase precipitate can also exhibit a lath-type morphology, but its interface will run along $\langle 150 \rangle_{Al}$ directions, see e.g. Ref. [31]. Alloy S did not show any clear presence of lath-type precipitates. Detailed characterisation of precipitate structures in the alloys studied here are presented in the related work by Sunde et al. [5]. This work also quantified the distribution of precipitate phases at different ageing conditions using a scanning diffraction approach.

The precipitate number density was calculated as $N = 3N_{\parallel}/(A(t + \bar{l}_m))$, where $N_{\parallel}$, is the number of precipitate cross-sections in the image, A is the field of view area, t is thickness in the centre of the image, and $\bar{l}_m$ is the average measured precipitate length. The factor 3 accounts for the 3 growth directions of the precipitates, hence assuming a uniform distribution. The volume fraction was subsequently calculated as $V_f = N \cdot \bar{l} \cdot \bar{a}$, where $\bar{l}$ and $\bar{a}$ denote the average precipitate length and cross-section area, respectively. N and V_f were calculated for all alloys for the conditions selected for TEM studies, and the results are shown in Fig. 7. All numerical values for the measured and calculated precipitate statistics are presented in Table SI 4, Table SI 5, and Table SI 6, for alloys S, C, and M, respectively.

As seen from Figs. 6 and 7, there were clear differences in precipitation between the alloys, despite their similar compositions and TMP. In terms of average precipitate parameters $\bar{l}$ and $\bar{a}$ (Fig. 6a and b), the rod-type precipitates of alloy M had consistently smaller dimensions as compared to the precipitates of alloys S and C, at the same ageing time. The lath-type precipitates of alloy M were longer than the precipitates of alloys S and C at 3 h and 24 h ageing. As seen from Fig. 7a, the lath-type precipitates of alloy M were in relatively low number densities at the corresponding ageing conditions. Lath-type precipitates were also present at the 1 month condition in alloy M, but the coarsened precipitates lying in-plane were not clearly separable as rods and laths (see Fig. 5i) and were therefore assumed to be approximately equal in size. Comparing the precipitates of alloy C to S, the length of the former stayed somewhat smaller for all corresponding conditions. The cross-section areas of the precipitates in alloy C also stayed smaller than for S up to 24 h ageing, but then became larger with significant overageing.

For a given ageing time, the precipitate number density (see Fig. 7a) was consistently highest in alloy M, followed by alloy C, and lastly S. The difference between alloy M as compared to both C and S became larger with prolonged ageing. For alloy M the number density of rod-type precipitates dropped off by more than an order of magnitude with ageing, whereas the lath-type precipitates stayed at the same order of magnitude even after 1 month ageing. The thermal resistance of lath-type precipitate phases, i.e. C and L phase, has also been demonstrated previously [1,32]. Comparing the number density for alloys C and S, it is seen that alloy C started out significantly higher than alloy S, but the difference decreased up to the point of moderate overageing (24 h). At the significantly OA state at 1 week ageing, alloy C was again higher in number density as compared to alloy S.

The volume fraction (see Fig. 7b) did not display as clear differences as were seen for the other precipitate statistical parameters. Note the uncertainties in calculated values. The main source of uncertainty is due to the thickness estimation by EELS ($\Delta t/t \approx 10\%$). The lower number density of precipitates in alloy S seems to be compensated by the increased size of precipitate parameters $\bar{l}$ and $\bar{a}$, making the volume fraction comparable to alloys C and M. The volume fraction of alloy C is

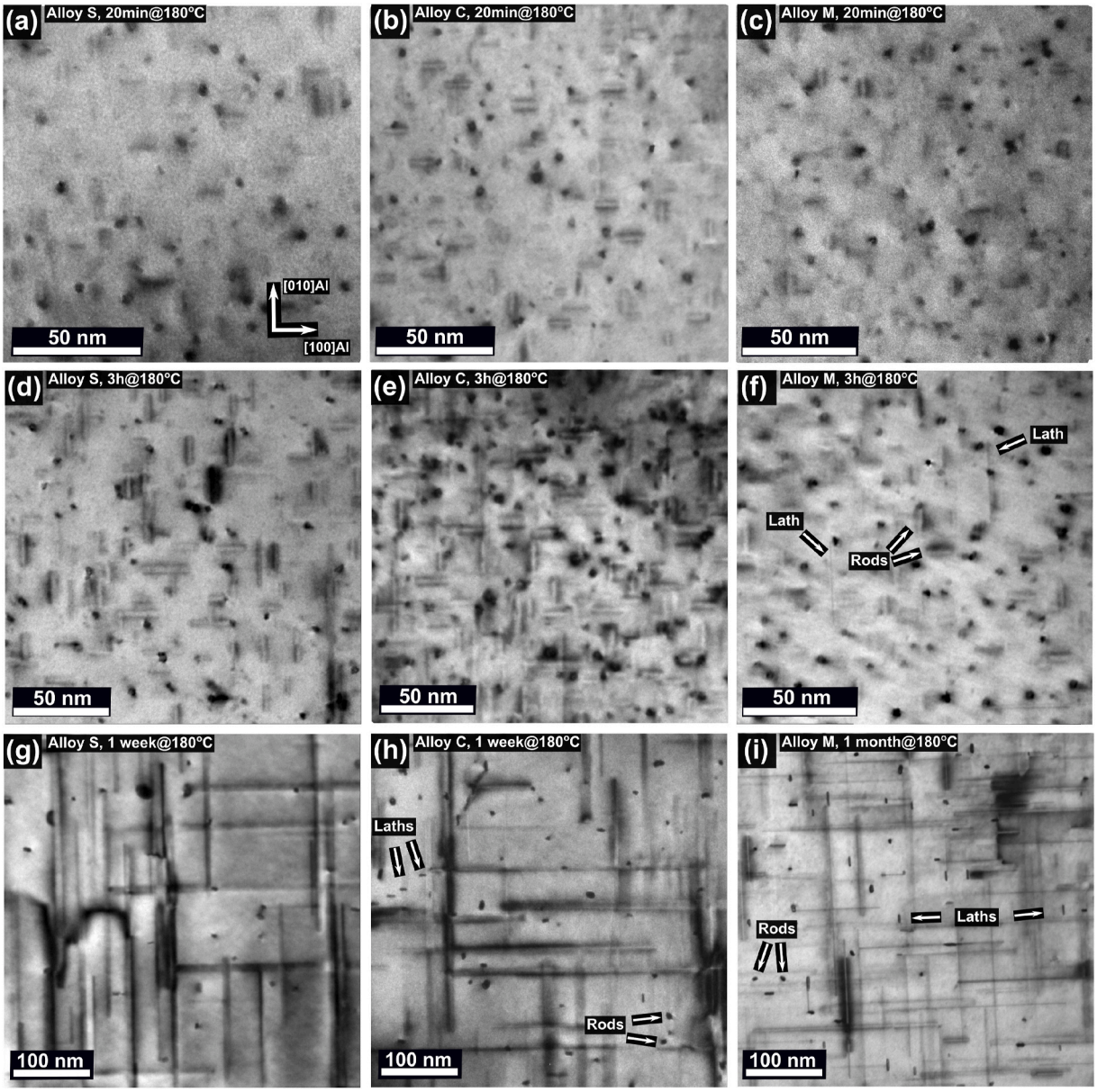

Fig. 5. (a–i) Bright-field TEM images of indicated alloys and ageing times. All images are acquired near the $[001]_{Al}$ zone axis.

similar to that of alloy M for the same reason, but the calculations indicate that the volume fraction of alloy M is somewhat larger up to the point of moderate overageing (24 h). It is also seen that for alloy M the lath-type precipitates were largest in number and volume over rod-type precipitates at the significantly OA condition (1 month).

The PFZ width perpendicular to GBs was also measured in each condition studied, see Fig. 8. The PFZ widths were nearly equal for alloys S and C, but differed notably for alloy M, being lower than all corresponding conditions in alloys S and C. After 1 month ageing there was a large difference between the PFZ width in alloy S at 267± 18 nm to that of alloy M at 172 ± 8 nm.

4. Discussion

4.1. Microstructure-property relationships

With few exceptions, it was generally observed that alloy M exhibited the highest strength and hardness with ageing, followed by alloy C, and lastly alloy S, see Figs. 3a and 4a. It was also generally observed from the microstructure results in Figs. 6 and 7 that alloy M showed the most refined precipitate microstructure, with smaller precipitate parameters, $\bar{l}$ and $\bar{a}$, and higher precipitate number densities, N. Alloy C places second and alloy S is last. Although the precipitates in alloy C at 1 week ageing had a larger cross-section area than those of alloy S, the average precipitate volume, $\overline{V}_p = \bar{l}\cdot\bar{a}$, was smaller for alloy C, which also had a slightly higher number density. The precipitate statistics of alloys S and C were closest in value between the 24 h and the 1 week ageing conditions, which were also the conditions where the measured hardness and strength were the most similar, see Figs. 3a and 4a.

At a fixed volume fraction, with precipitates of similar types and morphology, a denser distribution of smaller precipitates is generally stronger than a sparse distribution of coarse precipitates, due to the statistically increased number of dislocation pinning points in each slip plane. The observed refinement in precipitate microstructure thus supports alloy M having the highest strength, followed by alloy C, and lastly alloy S.

An exception not immediately explained by this reasoning is the slightly increased strength of alloy C as compared to alloy M between 1 h

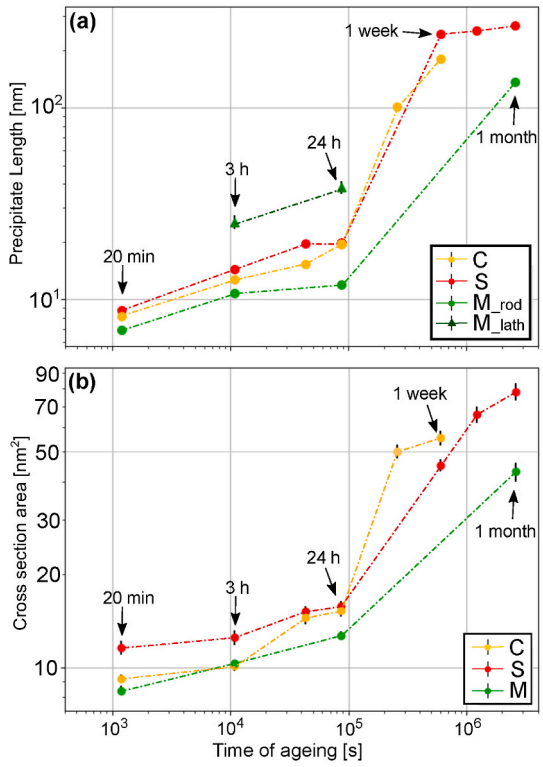

Fig. 6. (a) Average length and (b) cross-section area for precipitates in all ageing conditions studied in alloys S, C, and M.

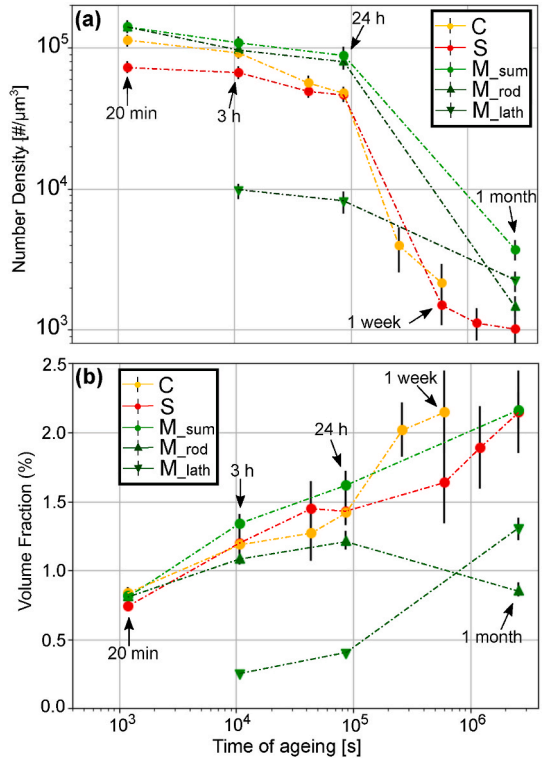

Fig. 7. (a) Precipitate number density and (b) precipitate volume fraction in each alloy and ageing condition studied.

and 5 h ageing. The calculated number densities at 3 h ageing were similar, at $(93 \pm 9) \cdot 10^3\ \mu m^{-3}$ compared to $(109 \pm 12) \cdot 10^3\ \mu m^{-3}$ for alloys C and M, respectively, and within the uncertainty of the measurement errors. Furthermore, the hardness seen in Fig. 3a showed that alloy M

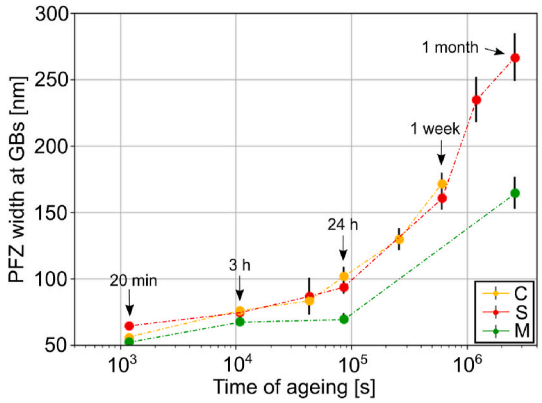

Fig. 8. Average measured PFZ width perpendicular to GBs in each alloy and ageing condition.

was harder than alloy C at all corresponding ageing conditions. The precipitate cross-section areas were comparable at UA and 3 h ageing, which implies that the obstacle strengths should be similar. However, as previously noted, alloy M also had a significant presence of lath-type precipitates, most notably L phase, which has a different aspect ratio and crystal structure than the β'' precipitate phase, and will therefore differ in dislocation obstacle strength. From microstructure observations it is therefore less evident how to explain the relative strength difference between alloys C and M at these conditions. As pointed out, it could be due to the uncertainties in measured precipitate statistics, or it could potentially indicate that L phase precipitates are weaker dislocation obstacles than β'' phase precipitates for smaller precipitate sizes.

With subsequent overageing, the number density of alloy M at 24 h and 1 month ageing was significantly higher than that of the corresponding OA conditions in alloys S and C, see Fig. 7. For alloy M, the precipitate parameters $\bar{l}$ and $\bar{a}$ did also not grow as fast as those of alloys S and C, see Fig. 6. This supports the measurement of a significantly higher material strength at these conditions. The conductivity plot seen in Fig. 3b also indicates that there occurred a slower coarsening of precipitates in alloy M beyond 24 h ageing relative to alloys S and C, as a lower conductivity normally correlates with a higher solute content in the matrix, and hence a reduced uptake of solutes in precipitates. It is also supported by the observation of a significantly reduced PFZ width at GBs in alloy M as compared to alloys S and C, see Fig. 8, which also indicated that more solutes remained in solid solution for alloy M as compared to alloys S and C with overageing.

The true fracture strain of the alloys remained similar up to the point of moderate overageing, at about 24 h, see Fig. 4b. After this point, there was a strong correlation between increased strength and a decreased fracture strain, as reported earlier [33]. Previous findings suggest that material ductility is mainly determined by the presence of larger, coarse particles in the alloys. It has for instance been demonstrated that coarse particles and precipitates on GBs are important sites for nucleation and growth of intergranular ductile fracture [34]. Some studies also point to the PFZ width as important for explaining ductility, as narrow PFZs may act to increase strain localisation and accelerate void nucleation and growth at GB particles [33,35]. The Fe content of the alloys studied here was nearly equal, see Table 1. Although not quantified, the similar processing parameters should therefore have resulted in similar distributions of primary particles in the three alloys. Alloy M had about half the Mn content and a much lower Cr content than alloys S and C, and therefore formed significantly fewer dispersoids, as seen qualitatively from low magnification ADF-STEM images. Based on the observed similarity in fracture strain up to the point of moderate overageing, the primary particles and the distribution of dispersoids were therefore not key in terms of determining material ductility.

Alloys S and C were the most similar in terms of composition, grain

structure, precipitate microstructure, and PFZ widths. At the 1 week ageing condition, the difference in fracture strain between alloys S and C measured $\Delta\varepsilon_f \approx 7\%$, with alloy S being the most ductile. At this condition, it was measured a higher number density of precipitates in alloy C than for S, obtained as 2153 and 1498 μm^{-3} for alloys C and S, respectively. The precipitates had a similar average volume in both alloys, see Fig. 6. This supported the measurement of a higher yield strength for alloy C than for S at this condition, obtained as 236 and 200 MPa for alloy C and S, respectively. Without any other notable differences in terms of material microstructure, the differences measured in fracture strain for all alloys were most likely due to the earlier nucleation of voids experienced by the strongest alloys, as explained in Ref. [36], which again is generally linked to the alloy with the highest number density of precipitates.

In summary, it was seen that a refinement of the precipitate distribution – with smaller precipitate parameters $\bar{l}$ and $\bar{a}$ and an increased density N of precipitates – correlated well with a higher material hardness and yield strength. The substantially retained strength of alloy M as compared to alloys S and C at OA conditions was seen as a consequence of the increased resistance towards coarsening and dissolution exhibited by the precipitates in this alloy. The formation of L phase precipitates is particularly important for explaining the observed differences, due to the improved thermal resistance of this phase as compared to the β'' phase [1,32]. This phase forms in alloy M because it is promoted by increased Mg/Si levels in combination with moderate additions of Cu (Cu≳0.1 at.%) [1,5]. Material ductility, assessed from measured fracture strain in the alloys, showed no significant differences up to the point of moderate overageing. After this point there was a strong correlation between increased strength and a decreased fracture strain.

4.2. Strength modelling

The study presented here is a suitable test case for modelling work. It provides material testing results and a quantification of the alloy microstructure at a range of ageing conditions from UA to significantly OA conditions. There exist many strengthening models for the AA6xxx series Al alloy system which attempt to link microstructure parameters, such as grain size, texture, precipitate size distribution, etc., to the macroscopic yield strength, σ_y. Several strengthening mechanisms are operative at room temperature, the most important of which is that due to the precipitates, σ_p. In addition, one must add the contribution from solid solution strengthening, σ_{ss}, as well as the intrinsic strength of pure Al, σ_i. If the latter is experimentally measured on a material of comparable grain size to that of the alloy under consideration, this also accounts for grain size strengthening effects. The contributions are typically added linearly [11,12]:

$$\sigma_y = \sigma_p + \sigma_{ss} + \sigma_i. \tag{1}$$

In estimating the solid solution strengthening, the contribution from each element is typically also added linearly, given as [6,37].

$$\sigma_{ss} = \sum_i k_i C_i^{\frac{2}{3}}, \tag{2}$$

where k_i is the scaling factor and C_i is the mass fraction of a specific element (i) in solid solution (wt.%).

The strengthening contribution from the distribution of precipitate needles and/or laths growing along $\langle 100\rangle_{Al}$ directions is more challenging to estimate. In the following, we have applied three selected models, see Table 3, for predicting the contribution σ_p. The NaMo, Esmaeili, and Holmedal models [11,13,15] have shown good agreement with selected experimental findings, and are recognised in the scientific literature. The models have here been modified as compared to their originally presented forms, with the intent to put them into a common framework, which is described in the work of Holmedal [15]. In the paper by Holmedal, the precipitate contribution to the stress is

Table 3
Strengthening models for estimating σ_p. For a detailed description of the models the cited works should be consulted.

Key equations	References
$n = \frac{3V_f}{2\pi\bar{r}_{eq}^2}$,	[10–12]
$f(r_{eq}) = \min\left(\frac{r_{eq}}{\bar{r}_{eq,3h}}, 1\right)$	(NaMo)
$n = \frac{V_f}{2\pi\bar{r}^2}$,	[9,13]
$\bar{f}(\bar{r}) = \min\left(\frac{\bar{r}}{\bar{r}_{3h}}, 1\right)$	(Esmaeili model)
$n = \frac{\sqrt{3}}{3}N\bar{l}$,	[15,27]
$f(a) = \min\left(\frac{a}{\bar{a}_{3h}}, 1\right)$	(Holmedal model)

calculated using Kocks statistics [7,8], which are based on numerical line-tension simulations of a dislocation gliding through an array of obstacles. Using recent line-tension simulations by Vaucorbeil et al. [38,39], Holmedal estimated the tensile stress using the following equation:

$$\sigma_p = M\tau = 0.9M(2\beta)\mu b\sqrt{n}\,\bar{f}^{\frac{3}{2}}\left(1 - \frac{1}{6}\bar{f}^5\right). \tag{3}$$

Here, M is the Taylor factor, τ is the critical resolved shear stress, μ is the shear modulus of the Al matrix, b is the length of the Burgers vector, and n is the density of obstacles per area slip plane. $\bar{f} = \bar{F}/2\beta\mu b^2 = \cos(\varphi_c/2)$ is the non-dimensional mean obstacle strength, where $\bar{F}$ is the mean obstacle strength, $\beta\mu b^2$ is the line tension of the dislocations, $\beta \approx 1/2$ is a constant, and φ_c is the obstacle breaking angle of the dislocation. Note that Eq. (3) is applied here for all models, replacing the Friedel statistics, $\sigma_p = M\mu b\sqrt{n\bar{f}^3}$, on which the original models by Deschamps and Brechet [10], Myhr et al. [11], and by Esmaeili et al. [13] were based. Note also that the two special cases of weak and strong obstacles in the Esmaeili model are here merged, using instead the approach by Holmedal. This makes the Esmaeili model more general, while its predictions remain essentially the same for the two special cases.

The way to derive the non-dimensional mean obstacle strength, $\bar{f}$, is slightly different for the considered models. The Esmaeili model can be regarded as a simplified version of the Holmedal model, where $\bar{f}$ is estimated simply as a function of the mean cross-sectional area of the precipitates. The approach by Holmedal takes into account the statistical distribution of the number of pinning points per particle, which depends on the length of the particle. In addition, the strength of pinning points, which depends on the particle's cross sectional area, is accounted for. This requires numerical integration of

$$\bar{f} = \frac{1}{N\bar{l}}\int f\varphi_l l dl, \tag{4}$$

for a strength, $f(a)$, and size distribution, φ_l, of precipitates with length l and cross-sectional area $a = l^2/\Omega^2$. Note that the size distribution here is not normalised, i.e. $\int \varphi_l dl = N$. It is assumed that the aspect ratio Ω is a function of l, i.e. a strong correlation between the length and cross-section area distributions. For a sufficiently narrow size distribution the Esmaeili and Holmedal models become equal.

The models by Deschamps and Brechet [10], and later the NaMo model [11], consider volume-equivalent spherical precipitates, for which $4\pi r_{eq}^3/3 = al$. For each precipitate, the obstacle strength is assumed to depend on its volume, i.e. a function $f(r_{eq})$, and the non-dimensional mean obstacle strength is integrated numerically from the precipitate size distribution as

$$\bar{f} = \frac{1}{N}\int f\varphi_{r_{eq}}\mathrm{d}r. \tag{5}$$

This integral does not account for the fact that larger particles pierce more glide planes and therefore contribute with more pinning points than smaller particles. An alternative expression for shearable spherical particles, similar to Eq. (4), may be found in Ref. [15]. However, since the particles considered in this work are not spherical anyway, this difference must be expected to be of second order. For the obstacle strengths, expressions similar as reported for the respective models were used, see Table 3.

TEM measurements gave distributions of precipitate lengths, l, and cross-section areas, a, at each studied ageing condition, with average values shown in Fig. 6. The distribution of precipitate lengths, φ_l , was found to be best fitted using a log-normal function

$$\varphi_l = \frac{N}{l\sqrt{2\pi\ln\left(1+s/\bar{l}^2\right)}}\exp\left(-\frac{\ln\left(l\sqrt{1+s/\bar{l}^2}/\bar{l}\right)^2}{2\ln\left(1+s/\bar{l}^2\right)}\right), \tag{6}$$

where s is the variance of the distribution. Generally, two precipitates of equal length may have different cross-section areas. The two are however correlated, and the aspect ratio $\Omega = l/\sqrt{a}$ may for simplicity be assumed to change as some function $\Omega(l)$ of the needle length, i.e. a direct correlation between the statistical distributions of needle lengths and cross-section areas. Using the average precipitate cross-section area, $\bar{a}$, and the average precipitate length, $\bar{l}$, measured at each ageing condition, the average precipitate aspect ratio was calculated as $\bar{\Omega} = \bar{l}/\sqrt{\bar{a}}$. A function $\Omega(l)$ was fitted to the calculated average values. The obtained function $\Omega(l)$ enabled conversion from measured distributions of precipitate lengths to cross-section areas and corresponding precipitate cross-section dimensions/radii. In order to apply the NaMo model, where the precipitates are assumed to be spherical, the radii were calculated by equating $V_{\text{sphere}} = \left(\frac{l}{\Omega(l)}\right)^2 \cdot l$, thereby converting to a distribution of volume equivalent spherical precipitates. A minor correction also had to be made to account for rod-shaped precipitates with a circular cross-section in the Esmaeili model, compared to square cross-sections in the Holmedal model.

Important for the application of all strengthening models is the critical dimension defining the transition point between shearable and non-shearable precipitates. This transition point was selected as the relevant dimension (cross-section area, length, or radius) calculated from the average precipitate parameters at 3 h ageing in each alloy, i.e. near peak strength.

The macroscopic yield strength for each alloy was calculated using Eq. (1). The intrinsic strength of pure Al, σ_i, was obtained experimentally, using the methodology and parameters described in the experimental section. The solid solution strengthening, σ_{ss}, was calculated using Eq. (2), where C_i for Mg, Si, and Cu were approximated from measured precipitate volume fractions, precipitate phase fractions as obtained by scanning precession electron diffraction (SPED) experiments, and reported precipitate phase chemical compositions, see SI 4. Using HyperSpy [40], the SPED data was decomposed using an unsupervised machine learning algorithm based on non-negative matrix factorization. The results were matched to (kinematically) simulated diffraction patterns of precipitate crystal structures in the Al–Mg–Si–Cu system, which enabled phase identification. Subsequently, precipitate

Table 4
Values used for model parameters.

Parameter	Value
σ_i	35 MPa [a]
k_{Si}, k_{Mg}, and k_{Cu}	66.3, 29.0, and 46.4 MPa/wt.% [b]
M	3.05 [c]
Alloy S: $\bar{r}_{eq,3h}$, $\bar{r}_{3h}$, $\bar{a}_{3h}$	3.54 nm, 3.54 nm, 12.45 nm^2
Alloy C: $\bar{r}_{eq,3h}$, $\bar{r}_{3h}$, $\bar{a}_{3h}$	3.25 nm, 3.18 nm, 10.13 nm^2
Alloy M: $\bar{r}_{eq,3h}$, $\bar{r}_{3h}$, $\bar{a}_{3h}$	2.97 nm, 3.21 nm, 10.29 nm^2
μ	19.8 GPa
β	0.47 [11]

[a] Obtained from tensile tests on pure aluminium.
[b] Taken from Ref. [11].
[c] Calculated from the measured extruded texture using the ALAMEL crystal plasticity model [42,43].

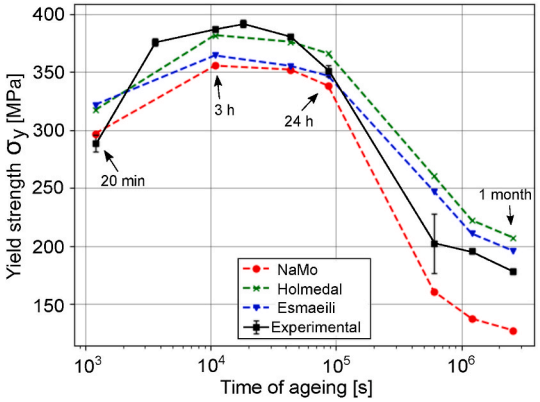

Fig. 9. Experimental results and model predictions of yield stress as a function of ageing for alloy S.

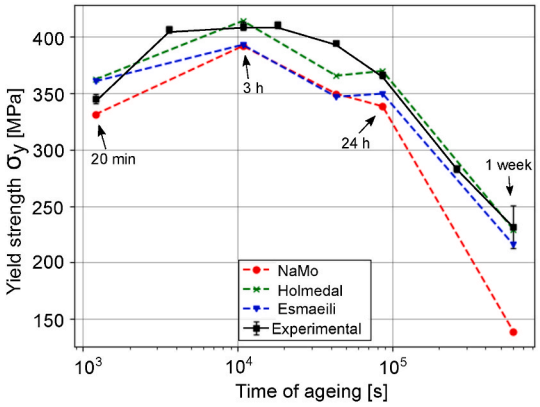

Fig. 10. Experimental results and model predictions of yield stress as a function of ageing for alloy C.

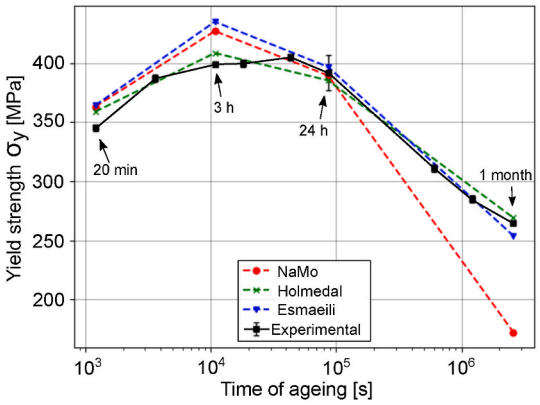

Fig. 11. Experimental results and model predictions of yield stress as a function of ageing for alloy M.

phase fractions were estimated using a pixel-based calculation where each precipitate PED pattern has been divided into a sum of the identified phase patterns. The details of this methodology and the calculation of C_i are explained in the related work by Sunde et al. [41]. Finally, the precipitate strengthening contribution, σ_p, was calculated by applying the three selected models. The parameter values used in the calculations are shown in Table 4.

Fig. 9, Fig. 10, and Fig. 11 show the comparison between the three applied models and the experimentally measured yield strength for alloys S, C, and M, respectively, for different ageing conditions. It is generally observed that the models capture the overall trend of the experimental results to a reasonable extent. The Holmedal model particularly obtains an excellent agreement for most conditions in all alloys. The Esmaeili model also generally shows a good agreement with experimental results. For alloys S and C it underestimates the strength up to the point of moderate overageing (24 h). For alloy M it overestimates the strength quite significantly at 3 h, where it predicts this to be the highest among all alloys and ageing conditions. The NaMo model obtains the best overall fit with the UA condition at 20 min ageing, and then mostly predicts a similar strength as the Esmaeili model up to the point of moderate overageing (24 h). Subsequently, at significantly OA conditions ($>$ 24 h ageing), the NaMo model underestimates the strength by $>$ 40 MPa for all conditions.

The underestimation of the strength at OA conditions by the NaMo model is most likely a consequence of the underlying simplification of using a spherical precipitate geometry. The geometry of a precipitate is important as it affects how many $\{111\}_{Al}$ slip planes a precipitate of a given volume V_p intersects. A spherical precipitate of radius r will act as a dislocation obstacle for a slip plane located within a distance $\pm r$ from the precipitate centre. A needle-shaped precipitate will act as a dislocation obstacle in any $\{111\}_{Al}$ slip plane located within a distance $\pm l\cos\theta = \pm l/\sqrt{3}$ from the precipitate centre, where $\theta = 54.74^\circ$ is the angle between the glide-plane normal and the needle direction. As seen from Fig. 6, the precipitates grow to reach lengths that are several 10s of times longer than their diameter/thickness, which implies that the strengthening effect per precipitate is greater for needle-shaped precipitates as compared to equivalent volume spherical precipitates. In the models applied this has consequences for the calculation of n, i.e. the density of obstacles per area slip plane.

The relative differences between the models and experimental results in the range 20 min $\leq t \leq$ 24 h show the same trend for alloys S and C shown in Figs. 9 and 10, and differ somewhat for alloy M, see Fig. 11. The similarities in the predictions for alloys S and C were expected, as the compositions of these alloys were very similar, and with both alloys showing a similar overall precipitation [5]. For alloy M, all models overestimate the strength at 3 h ageing, and the NaMo and Esmaeili models predict this as the highest among all alloys and ageing times. For the 3 h ageing condition in alloys S and C, the NaMo and Esmaeili models underestimate the strength. Part of the reason for this over- and underestimation of strength must lie in the observed coexistence of two precipitate classes, namely β'' and L phase precipitates, which was mainly observed in alloy M. It was measured a number density of roughly 10,000 and 100,000 μm^{-3} lath- and rod-type precipitates in alloy M at 3 h ageing, respectively, compared to 93,000 rod-type precipitates in alloy C ($\Delta N/N \approx 10\%$). The length of the rod-type precipitates in alloy C at 3 h ageing was somewhat longer than for alloy M, at 12.6 nm compared to 10.7 nm, respectively, and with nearly equal cross-section areas.

Because the NaMo and Esmaeili models overestimate the strength of alloy M at 3 h ageing, this suggests that a significant fraction of the precipitates at this condition should still be considered weak, and therefore that the critical radius, $r_c > r_{3h}$. The differences in the crystal structures of the β'' and L phase precipitates imply that they will have different critical cross-section areas or radii defining the shearable/non-shearable transition point. These were assumed to be equal in the calculations presented here, and set to the average value measured. In the discussion of the strength comparison between alloys C and M at 3 h ageing, see section 4.1, it was suggested that the L phase precipitates may be weaker dislocation obstacles than the β'' precipitates at moderately aged conditions ($t < t_{peak}$). This is also indicated here in the comparison to modelling results. Simulations of interactions between moving dislocations and β'' and L phase precipitates at the atomic level would provide more insight into this observation.

5. Conclusions

A combination of mechanical testing, TEM precipitate microstructure quantification, and strength modelling have been applied to better understand material-property relationships in three Al-Mg-Si(-Cu) alloys of similar compositions at a range of ageing conditions.

It was found that relatively small changes in alloy compositions caused significant differences in the precipitate microstructures, with corresponding significant differences in the measured material properties, including yield strength and fracture strain. The Mg-rich and highest Cu content alloy M generally showed the highest strength with ageing. This was explained based on an increased refinement of the precipitate microstructure, with higher number densities of smaller precipitates at all ageing conditions, as compared to the more Si-rich alloys S and C. Furthermore, alloy M also formed lath-shaped L phase precipitates with high aspect ratios, exhibiting large resistance towards dissolution/coarsening, which was the main explanation for a significantly improved thermal stability for alloy M as compared to S and C. Comparing alloys S and C, the higher Cu content of alloy C caused an increased refinement of the precipitate microstructure, with resulting higher strength than for alloy S. The highest yield strengths obtained were 392, 410, and 406 MPa for alloys S, C, and M, respectively. Three strengthening models were applied using the calculated precipitate statistics and the results showed generally good agreement with experimental results. Material ductility remained comparable for all alloys up to moderate overageing, and then a higher material strength corresponded with a lower material ductility. The difference became progressively larger with further overageing.

It is the authors' intent that the large body of data presented in this study should encourage further studies and developments, particularly on the aspect of precipitation and strength modelling work for the Al-Mg-Si-Cu system.

CRediT authorship contribution statement

Jonas K. Sunde: Conceptualization, Methodology, Investigation, Modelling, Writing - original draft, Writing - review & editing. **Feng Lu:** Conceptualization, Methodology, Investigation, Modelling. **Calin D. Marioara:** Conceptualization, Methodology, Investigation, Writing - review & editing. **Bjørn Holmedal:** Conceptualization, Methodology, Modelling, Writing - review & editing. **Randi Holmestad:** Conceptualization, Supervision, Writing - review & editing.

Declaration of competing interest

The authors declare that they have no known competing financial interests or personal relationships that could have appeared to influence the work reported in this paper.

Acknowledgements

All authors acknowledge support from the AMPERE project (NFR 247783), a knowledge building project for industry, co-financed by The Research Council of Norway (NFR), and the industrial partners Hydro, Gränges, Neuman Aluminium Raufoss (Raufoss Technology), and Nexans. The TEM work was carried out on the NORTEM infrastructure (NFR

197405) at the TEM Gemini Centre, Trondheim, Norway.

Appendix A. Supplementary data

Supplementary data to this article can be found online at https://doi.org/10.1016/j.msea.2021.140862.

Data availability

The Supplementary Information following this publication presents tensile test data, parameters of Voce equation fitted flow stress-strain curves until fracture, numerical values for TEM precipitate statistics, fitting of precipitate length distribution data, and estimated solid solution levels at each ageing condition.

References

[1] C.D. Marioara, S.J. Andersen, J. Røyset, O. Reiso, S. Gulbrandsen-Dahl, T.-E. Nicolaisen, I.-E. Opheim, J.F. Helgaker, R. Holmestad, Improving thermal stability in Cu-containing Al–Mg–Si alloys by precipitate optimization, Metall. Mater. Trans. 45 (2014) 2938–2949.

[2] G.A. Edwards, K. Stiller, G.L. Dunlop, M.J. Couper, The precipitation sequence in Al-Mg-Si alloys, Acta Mater. 46 (11) (1998) 3893–3904.

[3] C. Cayron, L. Sagalowicz, L. Sagalowicz, P.A. Buffat, Structural phase transition in Al-Cu-Mg-Si alloys by transmission electron microscopy study on an Al-4 wt% Cu-1 wt% Mg-Ag alloy reinforced by SiC particles, Philos. Mag. A 79 (11) (1999) 2833–2851.

[4] C.D. Marioara, S.J. Andersen, T.N. Stene, H. Hasting, J. Walmsley, A.T.J. Van Helvoort, R. Holmestad, The effect of Cu on precipitation in Al-Mg-Si alloys, Phil. Mag. 87 (23) (2007) 3385–3413.

[5] J.K. Sunde, C.D. Marioara, R. Holmestad, The effect of low Cu additions on precipitate crystal structures in overaged Al-Mg-Si(-Cu) alloys, Mater. Char. 160 (2020) 110087.

[6] J. Friedel, Dislocations, vol. 1, Pergamon Press, Oxford, UK, 1964.

[7] U.F. Kocks, A statistical theory of flow stress and work-hardening, Phil. Mag. 13 (1966) 541–566.

[8] A.S. Argon, U.F. Kocks, M.F. Ashby, Thermodynamics and kinetics of slip, Prog. Mater. Sci. 19 (1975) 1–281.

[9] B.C. Muddle, J.F. Nie, I.J. Polmear, The effect of precipitate shape and orientation on dispersion strengthening in high strength aluminium alloys, Mater. Sci. Forum 530 (1996) 217–222.

[10] A. Deschamps, Y. Brechet, Influence of predeformation and ageing of an Al–Zn–Mg alloy–II. Modeling of precipitation kinetics and yield stress, Acta Mater. 47 (1) (1998) 293–305.

[11] O.R. Myhr, Ø. Grong, S.J. Andersen, Modelling of the age hardening behaviour of Al–Mg–Si alloys, Acta Mater. 49 (1) (2001) 65–75.

[12] O.R. Myhr, Ø. Grong, K.O. Pedersen, A combined precipitation, yield strength, and work hardening model for Al–Mg–Si alloys, Metall. Mater. Trans. 41 (2010) 2276–2289.

[13] S. Esmaeili, D.J. Lloyd, W.J. Poole, A yield strength model for the Al–Mg–Si–Cu alloy AA6111, Acta Mater. 51 (8) (2003) 2243–2257.

[14] A. Bahrami, A. Miroux, J. Sietsma, An age-hardening model for Al-Mg-Si alloys considering needle-shaped precipitates, Metall. Mater. Trans. 43 (11) (2012) 4445–4453.

[15] B. Holmedal, Strength contributions from precipitates, Phil. Mag. Lett. 95 (12) (2015) 594–601.

[16] M. Yang, H. Chen, A. Orekhov, Q. Lu, X. Lan, K. Li, S. Zhang, M. Song, Y. Kong, D. Schryvers, Y. Du, Quantified contribution of β'' and β' precipitates to the strengthening of an aged Al-Mg-Si alloy, Mater. Sci. Eng. 774 (2020) 138776.

[17] J. Jansen, C. Træholt, U. Tundal, S.J. Andersen, H.W. Zandbergen, O. Reiso, The crystal structure of the β'' phase in Al–Mg–Si alloys, Acta Mater. 46 (9) (1998) 3283–3298.

[18] J. Ribis, A. Lopez, K. Buchanan, K. Colas, J. Garnier, Analysis of the metastable precipitates in peak-hardness aged Al-Mg-Si(-Cu) alloys with differing Si contents, Acta Mater. 132 (2017) 209–221.

[19] M. Vivas, P. Lours, C. Levaillant, A. Couret, M.-J. Casanove, A. Coujou, Determination of precipitate strength in aluminium alloy 6056-T6 from transmission electron microscopy in situ straining data, Philos. Mag. A 76 (5) (1997) 921–931.

[20] F. Delmas, M. Vivas, P. Lours, M.-J. Casanove, A. Couret, A. Coujou, Straining mechanisms in aluminium alloy 6056. in-situ investigation by transmission electron microscopy, Mater. Sci. Eng. 340 (1) (2003) 286–291.

[21] Ø. Ryen, B. Holmedal, K. Marthinsen, T. Furu, Precipitation, strength and work hardening of age hardened aluminium alloys, IOP Conf. Ser. Mater. Sci. Eng. 89 (2015), 012013.

[22] K. Misumi, K. Kaneko, T. Nishiyama, T. Maeda, K. Yamada, K. Ikeda, M. Kikuchi, K. Takata, M. Saga, K. Ushioda, Three-dimensional characterization of interaction between β'' precipitate and dislocation in Al–Mg–Si alloy, J. Alloys Compd. 600 (2014) 29–33.

[23] W.J. Poole, X. Wang, D.J. Lloyd, J.D. Embury, The shearable–non-shearable transition in Al–Mg–Si–Cu precipitation hardening alloys: implications on the distribution of slip, work hardening and fracture, Phil. Mag. 85 (26–27) (2005) 3113–3135.

[24] E. Christiansen, C.D. Marioara, B. Holmedal, O.S. Hopperstad, R. Holmestad, Nano-scale characterisation of sheared β'' precipitates in a deformed aluminium alloy, Sci. Rep. 9 (1) (2019) 17446.

[25] K. Teichmann, C.D. Marioara, S.J. Andersen, K. Marthinsen, TEM study of β' precipitate interaction mechanisms with dislocations and β' interfaces with the aluminium matrix in Al–Mg–Si alloys, Mater. Char. 75 (1–7) (2013).

[26] A.L. Dons, E.K. Jensen, Y. Langsrud, E. Tromborg, S. Brusethaug, The Alstruc microstructure solidification model for industrial aluminum alloys, Metall. Mater. Trans. 30 (8) (1999) 2135–2146.

[27] Lu, F., Mánik, T., Andersen, I.L., Holmedal, B., A robust image processing algorithm for optical based stress-strain curve corrections after necking. (Submitted, 2021).

[28] N. Gromada, G. Mishuris, A. Öchsner, Correction Formulae for the Stress Distribution in Round Tensile Specimens at Neck Presence, Springer, Berlin, Heidelberg, 2011.

[29] S.J. Andersen, Quantification of the Mg_2Si β'' and β' phases in AlMgSi alloys by transmission electron microscopy, Metall. Mater. Trans. 26 (8) (1995) 1931–1937.

[30] M. Torsæter, W. Lefebvre, C.D. Marioara, S.J. Andersen, J.C. Walmsley, R. Holmestad, Study of intergrown L and Q' precipitates in Al–Mg–Si–Cu alloys, Scripta Mater. 64 (9) (2011) 817–820.

[31] C.D. Marioara, J. Friis, E. Hersent, A. Oskarsson, A transmission electron microscopy study of precipitate phases that form during operation in a heat exchanger alloy, Mater. Char. 149 (2019) 218–225.

[32] J.K. Sunde, S. Wenner, R. Holmestad, In situ heating TEM observations of evolving nanoscale Al-Mg-Si-Cu precipitates, J. Microsc. 279 (3) (2020) 143–147.

[33] B.H. Frodal, E. Christiansen, O.R. Myhr, O.S. Hopperstad, The role of quench rate on the plastic flow and fracture of three aluminium alloys with different grain structure and texture, Int. J. Eng. Sci. 150 (2020) 103257.

[34] A.K. Vasudévan, R.D. Doherty, Grain boundary ductile fracture in precipitation hardened aluminum alloys, Acta Metall. 35 (6) (1987) 1193–1219.

[35] K. Marthinsen, O.S. Hopperstad, E. Christiansen, C.D. Marioara, R. Holmestad, Lattice rotations in precipitate free zones in an Al-Mg-Si alloy, Mater. Char. 144 (2018) 522–531.

[36] A. Simar, K.L. Nielsen, B. de Meester, V. Tvergaard, T. Pardoen, Micro-mechanical modelling of ductile failure in 6005a aluminium using a physics based strain hardening law including stage iv, Eng. Fract. Mech. 77 (13) (2010) 2491–2503.

[37] F.R.N. Nabarro, Theory of Crystal Dislocations, Oxford University Press, Oxford, 1967.

[38] A. de Vaucorbeil, W.J. Poole, C.W. Sinclair, The superposition of strengthening contributions in engineering alloys, Mater. Sci. Eng. 582 (2013) 147–154.

[39] A. de Vaucorbeil, W.J. Poole, C.W. Sinclair, The effect of obstacle strength distribution on the critical resolved shear stress of engineering alloys, Mater. Sci. Forum 794–796 (2014) 449–454.

[40] F. de la Peña, et al., Hyperspy/Hyperspy: v1.6.1, 2020.

[41] J.K. Sunde, C.D. Marioara, A.T.J. van Helvoort, R. Holmestad, The evolution of precipitate crystal structures in an Al-Mg-Si(-Cu) alloy studied by a combined HAADF-STEM and SPED approach, Mater. Char. 142 (2018) 458–469.

[42] P. Van Houtte, S. Li, M. Seefeldt, L. Delannay, Deformation texture prediction: from the taylor model to the advanced lamel model, Int. J. Plast. 21 (3) (2005) 589–624.

[43] K. Zhang, B. Holmedal, T. Mánik, A. Saai, Assessment of advanced taylor models, the taylor factor and yield-surface exponent for fcc metals, Int. J. Plast. 114 (2019) 144–160.